Deep Rigid Instance Scene Flow

Wei-Chiu Ma[1,2] Shenlong Wang[1,3] Rui Hu[1] Yuwen Xiong[1,3] Raquel Urtasun[1,3]
[1]Uber Advanced Technologies Group
[2]Massachusetts Institute of Technology
[3]University of Toronto

Abstract

In this paper we tackle the problem of scene flow estimation in the context of self-driving. We leverage deep learning techniques as well as strong priors as in our application domain the motion of the scene can be composed by the motion of the robot and the 3D motion of the actors in the scene. We formulate the problem as energy minimization in a deep structured model, which can be solved efficiently in the GPU by unrolling a Gaussian-Newton solver. Our experiments in the challenging KITTI scene flow dataset show that we outperform the state-of-the-art by a very large margin, while being 800 times faster[1].

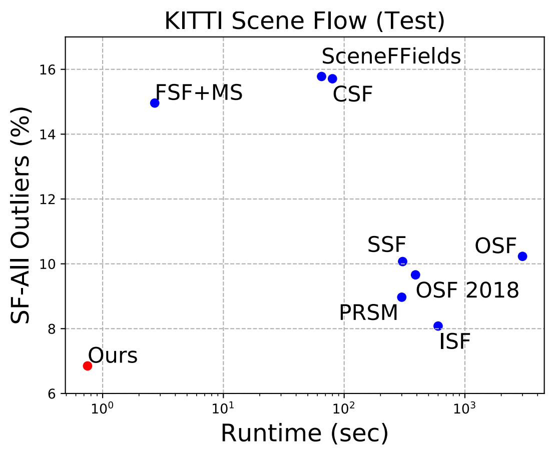

Figure 1: **Performance vs runtime on KITTI SceneFlow dataset:** Our approach is much faster and more accurate.

1. Introduction

Scene flow refers to the problem of estimating a three-dimenional motion field from a set of two consecutive (in time) stereo pairs. It was first introduced in [40] to describe the 3D motion of each point in the scene. Through scene flow, we can gain insights into the geometry as well as the overall composition and motion of the scene. It is of particular importance for robotics systems, such as self-driving cars, as knowing the 3D motion of other objects in the scene can not only help the autonomous systems avoid collision while planing its own future movements, but also improve the understanding of the scene and predict the intent of others. In this work, we focus on estimating the 3D scene flow in autonomous driving scenarios.

In the world of self-driving, the motion of the scene can be mostly explained by the motion of the ego-car. The presence of dynamic objects which typically move rigidly can also be utilized as strong priors. Previous structure prediction approaches often exploit these facts and fit a piece-wise rigid representations of motion [41, 44, 28, 4]. While these methods achieve impressive results on scene flow estimation, they require minutes to process each frame, and thus cannot be employed in real-world robotics systems.

On the other hand, deep learning based methods have achieved state-of-the-art performance in real time on a variety of low level tasks, such as optical flow prediction [12, 32, 38] and stereo estimation [46, 27, 25]. While they produce 'accurate' results, their output is not structured and cannot capture the relationships between estimated variables. For instance, they lack the ability to guarantee that pixels on a given object produce consistent estimates. While this phenomenon may have little impact in photography editing applications, this can cathastrophic in the context of self-driving cars, where the motion of the full object is more important than the motion of each individual pixel.

With these problems in mind, we develop a novel deep rigid instance scene flow (DRISF) model that takes the best of both worlds. The idea behind is that the motion of the scene can be composed by estimating the 3D rigid motion of each actor. The static background can also be modeled as a rigidly moving object, as its 3D motion can be described by the 'ego-car' motion. The problem is thus reduced to estimating the 3D motion of each traffic participant. Towards this gaol, we first capitalize on deep neural networks to esti-

[1]The uncompressed version of this paper can be found at http://bit.ly/CVPR-DRISF

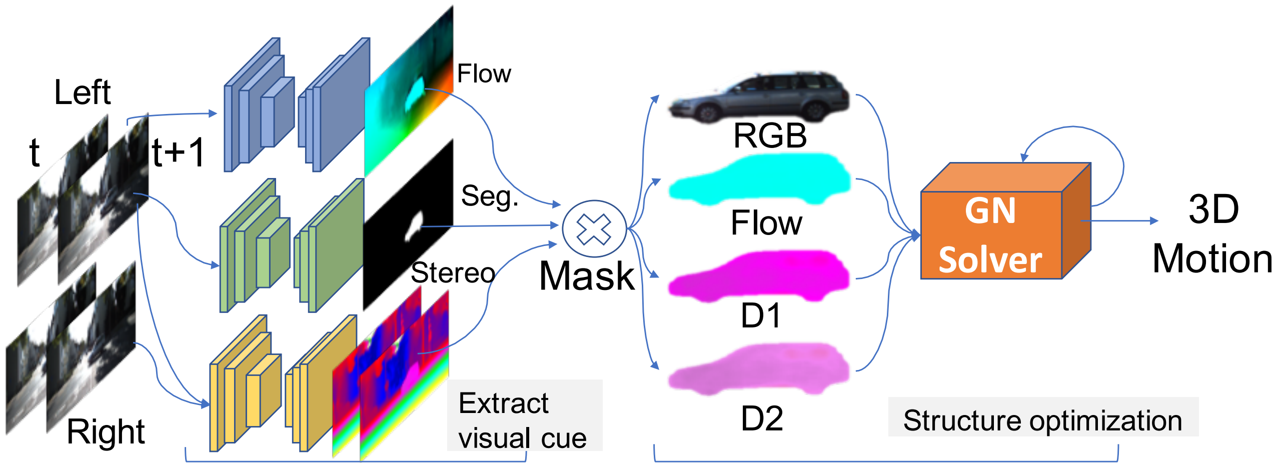

Figure 2: **Overview of our approach:** Given two consecutive stereo images, we first estimate the flow, stereo, and segmentation (Sec. 3.1). The visual cues of each instance are then encoded as energy functions (Sec. 3.2) and passed into the Gaussian-Newton (GN) solver to find the best 3D rigid motion (Sec. 3.3). The GN solver is unrolled as a recurrent network.

mate optical flow, disparity and instance segmentation. We then exploit multiple geometry based energy functions to encode the structural geometric relationship between these visual cues. Through optimizing the energy function, we can effectively reason about the 3D motion of each traffic participant. As the energy takes the form of weighted sum of squares, it can be efficiently minimized via Gaussian-Newton (GN) algorithm [6]. We implement the GN solver as layers in neural networks, thus all operations can be computed efficiently on the GPU in an end-to-end fashion.

We demonstrate the effectiveness of our approach on the KITTI scene flow dataset [28]. As shown in Fig. 1, our deep rigid instance scene flow model outperforms all previous methods by a significant margin in both runtime and accuracy. Importantly, it achieves state-of-the-art performance on almost every entry. Comparing to prior art, DRISF reduces the D1 outliers ratio by **43%**, the D2 outliers ratio by **32%**, and the flow outliers ratio by **24%**. Comparing to the existing best scene flow model [4], our scene flow error is **22%** lower and our runtime is **800** times faster.

2. Related Work

Optical flow: Optical flow is traditionally posed as an energy minimization task. It dates back to Horn and Schunck [18] where they define the energy as a combination of a data term and a smoothness term, and adopt variational inference to solve it. Since then, a variety of improvements have been proposed [7, 5, 30]. Recently, deep learning has replaced the variational approaches. Employing deep features for matching [2, 43] improved performance by a large margin. However, as the matching results are not dense, post-processing steps are required [35]. This not only reduces the speed, but also limits the overall performance.

Pioneered by Flownet [12], a variety of end-to-end deep regression based methods have been proposed [22]. Flownet2 [21] stacks multiple networks to iteratively refine the estimated flow and introduces a differentiable warping operation to compensate for large displacements. As the resulting network is very large, SpyNet [32] propose to use spatial pyramid network to handle large motions. They reduce the model size greatly, yet at the cost of degrading performance. Lite-Flownet [20] and PWC-Net [38, 37] extend this idea and incorporate the traditional pyramid processing and cost volume concepts into the network. Comparing to previous approach, the resulting model is smaller and faster. In this work, we adapt the latest PWC-Net as our flow module.

Stereo: Traditional stereo methods [17, 23] follow three steps: compute patch-wise feature, construct cost volumes, and final post-processing. The representation of the patch plays an important role. Modern approaches leverage CNNs to predict whether two patches are a match [45, 46]. While they showed great performance in challenging benchmarks, they are computationally expensive. To speed up the matching process, Luo *et al*. [25] propose a siamese matching network which exploits a correlation layer [10] to extract marginal distributions over all possible disparities. While the usage of the correlation layer significantly improves efficiency, they still require post-processing techniques [16, 47] to smooth their estimation, which largely limits their speed. In light of this, networks that directly regress sub-pixel disparities from the given stereo image pair have been proposed. DispNet [27] exploits a 1D correlation layer to approximate the stereo cost volumes and rely on later layers

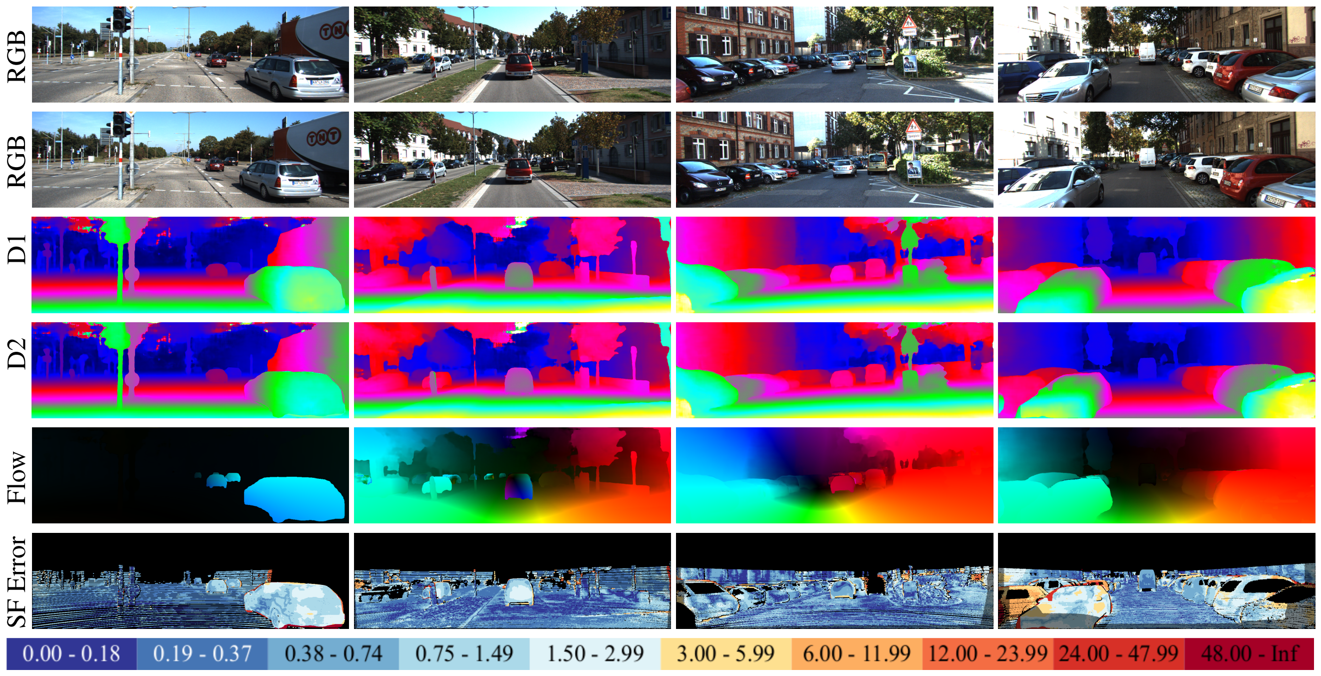

Figure 3: **Qualitative results on val set:** Our model can estimate the background motion very accurately. It is also able to estimate the 3D motion of foreground objects in most scenarios. It fails in challenging cases as show in last column.

for implicit aggregation. Kendall *et al.* [24] incorporate 3D conv for further regularization and propose a differentiable soft argmin to enable sub-pixel disparity from cost volumes. PSM-Net [9] later extend [24] by incorporating stacked hourglass [29] and Pyramid spatial pooling [48, 15]. In this work, we exploit PSM-Net as our stereo module.

Scene flow: Scene flow [40] characterizes the 3D motion of a point. Similar to optical flow estimation, the task is traditionally formulated as a variational inference problem [39, 31, 19, 3]. However, the performance is rather limited in real world scenarios due to errors caused by large motions. To improve the robustness, slanted-plane based methods [44, 28, 41, 26] propose to decompose the scene into small rigidly moving planes and solve the discrete-continuous optimization problem. Behl *et al.* [4] build upon [28], and incorporate recognition cues. With the help of fine-grained instance and geometric feature, they are able to establish correspondences across various challenging scenarios. Similar to our work, Ren *et al.* [34] exploit multiple visual cues for scene flow estimation. They encode the features via a cascade of conditional random fields and iteratively refine them. While these methods have achieved impressive performance, they are computationally expensive for practical usage. Most methods require minutes to compute one scene flow. This is largely due to the complicated optimization task. In contrast, our deep structured motion estimation model is able to compute scene flow in less than a second, which is two to three orders of magnitude faster than existing approaches.

3. Deep Rigid Instance Scene Flow

In this paper we are interested in estimating scene flow in the context of self-driving cars. We build our model on the intuition that in this scenario the motion of the scene can be formed by estimating the 3D motion of each actor. The static background can be also modeled as a rigidly moving object, as its 3D motion can be described by the 'ego-car' motion. Towards this goal, we proposed a novel deep structured model that exploits optical flow, stereo, as well as instance segmentation as visual cues. We start by describing how we employ deep learning to effectively estimate the geometric and semantic features. We then formulate the scene flow task as an energy minimization problem and discuss each energy term in details. Finally, we describe how to perform efficient inference and learning.

3.1. Visual Cues

We exploit three types of visual cues: instance segmentation, optical flow and stereo.

Instance Segmentation: We utilize Mask R-CNN [14] as our instance segmentation network, as it produces state-of-the-art results in autonomous driving benchmarks such as

		Disparity 1			Disparity 2			Optical Flow			Scene Flow		
Methods	Runtime	*bg*	*fg*	all	*bg*	*fg*	all	*bg*	*fg*	all	*bg*	*fg*	all
CSF [26]	1.3 mins	4.57	13.04	5.98	7.92	20.76	10.06	10.40	25.78	12.96	12.21	33.21	15.71
OSF [28]	50 mins	4.54	12.03	5.79	5.45	19.41	7.77	5.62	18.92	7.83	7.01	26.34	10.23
SSF [34]	5 mins	3.55	8.75	4.42	4.94	17.48	7.02	5.63	14.71	7.14	7.18	24.58	10.07
OSF-TC* [1]	50 mins	4.11	9.64	5.03	5.18	15.12	6.84	5.76	13.31	7.02	7.08	20.03	9.23
PRSM* [42]	5 mins	3.02	10.52	4.27	5.13	15.11	6.79	5.33	13.40	6.68	6.61	20.79	8.97
ISF [4]	10 mins	4.12	6.17	4.46	4.88	11.34	5.95	5.40	**10.29**	6.22	6.58	**15.63**	8.08
Our DRISF	**0.75 sec**	**2.16**	**4.49**	**2.55**	**2.90**	**9.73**	**4.04**	**3.59**	10.40	**4.73**	**4.39**	15.94	**6.31**

Table 1: **Comparison against top 5 published approaches:** Our method acheives state-of-the-art performance on almost every entry while being two to three orders of magnitude faster. (*: Method uses more than two temporally adjacent images.)

KITTI [13] and Cityscapes [11]. Mask R-CNN is a proposal based two stage network built upon Faster R-CNN [33]. For each object proposal, it predicts the object class, regresses its 2D box, and infers the bg/fg segmentation mask.

Stereo: We exploit the pyramid stereo matching network (PSM-Net) [9] to compute our stereo estimates. It consists of three main modules: fully convolutional feature module, spatial pyramid pooling [15, 48] and 3D cost volume processing. The feature module computes a high-dimensional feature map in a fully convolutional manner; the spatial pyramid pooling aggregates context in different scales and locations to construct the cost volume; the 3D cost volume module then performs implicit cost volume aggregation and regularizes it using stacked hourglass networks. Compared to previous disparity regression networks, PSM-Net learns to refine and produce sharp disparity images that respect object boundaries better. This is of crucial importance as over-smoothed results often deteriorates motion estimation.

Optical Flow: Our flow module is akin to PWC-Net [38], which is a state-of-the-art flow network designed based on three classical principles (similar to stereo networks): pyramidal feature processing, warping, and cost volume reasoning. Pyramidal feature processing encode visual features with large context; the progressive warping reduces the cost of building cost-volume through a coarse-to-fine scheme. Cost volume reasoning further boost performance by sharpening the boundaries. We implement PWC-net with one modification: during the warping operation, we use the feature of the nearest boundary pixel to pad if the sampling point falls outside the image, rather than 0. Empirically we found this to improve performance.

3.2. Energy Formulation

We now describe the energy formulation of our deep structured model. Let $\mathcal{L}^0, \mathcal{R}^0, \mathcal{L}^1, \mathcal{R}^1$ be the input stereo pairs captured from two consecutive time steps. Let $\mathcal{D}^0, \mathcal{D}^1$ be the estimated stereo, and $\mathcal{F}_\mathcal{L}, \mathcal{F}_\mathcal{R}$ be the inferred flow. Denote $\mathcal{S}^0_\mathcal{L}$ as the instance segmentation computed on the left image $\mathcal{L}^0$. Assume all cameras are pre-calibrated with known intrinsics. We parametrize the 3D rigid motion with $\boldsymbol{\xi} \in \mathfrak{se}(3)$, the Lie-algebra associated with $SE(3)$. We use this parametrization as it is a minimal representation for 3D motion. For each instance $i \in \mathcal{S}^0_\mathcal{L}$, we aim to find the rigid 3D motion that minimizes the weighted combination of photometric error, rigid fitting and flow consistency, where the weights are denoted as $\lambda_{\cdot,i}$. For simplicity, let $\mathcal{I} = \{\mathcal{L}^0, \mathcal{R}^0, \mathcal{L}^1, \mathcal{R}^1, \mathcal{D}^0, \mathcal{D}^1, \mathcal{F}_\mathcal{L}, \mathcal{F}_\mathcal{R}\}$ be input images and visual cues. We denote the set of pixels belonging to instance i as $P_i = \{\boldsymbol{p} | S^0_\mathcal{L}(\boldsymbol{p}) = i\}$. Note that background can be considered as an 'instance' since all the pixels in it undergo the same rigid transform. We obtain the 3D motion of each instance by minimizing

$$\min_{\boldsymbol{\xi}} \{\lambda_{\text{photo},i} E_{\text{photo},i}(\boldsymbol{\xi}; \mathcal{I}) + \lambda_{\text{rigid},i} E_{\text{rigid},i}(\boldsymbol{\xi}; \mathcal{I}) + \lambda_{\text{flow},i} E_{\text{flow},i}(\boldsymbol{\xi}; \mathcal{I})\} \quad (1)$$

The three energy terms are complementary. They capture the geometry and appearance agreement between the observations and inferred rigid motion. Next, we describe the energy terms in more details.

Photometric Error: This energy encodes the fact that correspondences should have similar appearance across all images. In particular, for each pixel $\boldsymbol{p} \in P_i$ in the reference image, we compare its photometric value with that of the corresponding pixel in the target image:

$$E_{\text{photo},i}(\boldsymbol{\xi}; \mathcal{I}) = \sum_{\boldsymbol{p} \in P_i} \alpha_{\boldsymbol{p}} \rho(\mathcal{L}^0(\boldsymbol{p}) - \mathcal{L}^1(\boldsymbol{p}')) \quad (2)$$

where $\alpha_{\boldsymbol{p}} \in \{0, 1\}$ is an indicator function representing which pixel is an outlier. We refer the reader to section 3.3 for a discussion on how to estimate α_p. $\boldsymbol{p}$ is a pixel in the reference image and $\boldsymbol{p}'$ stands for the projected image coordinate on another image, given by inverse depth warping

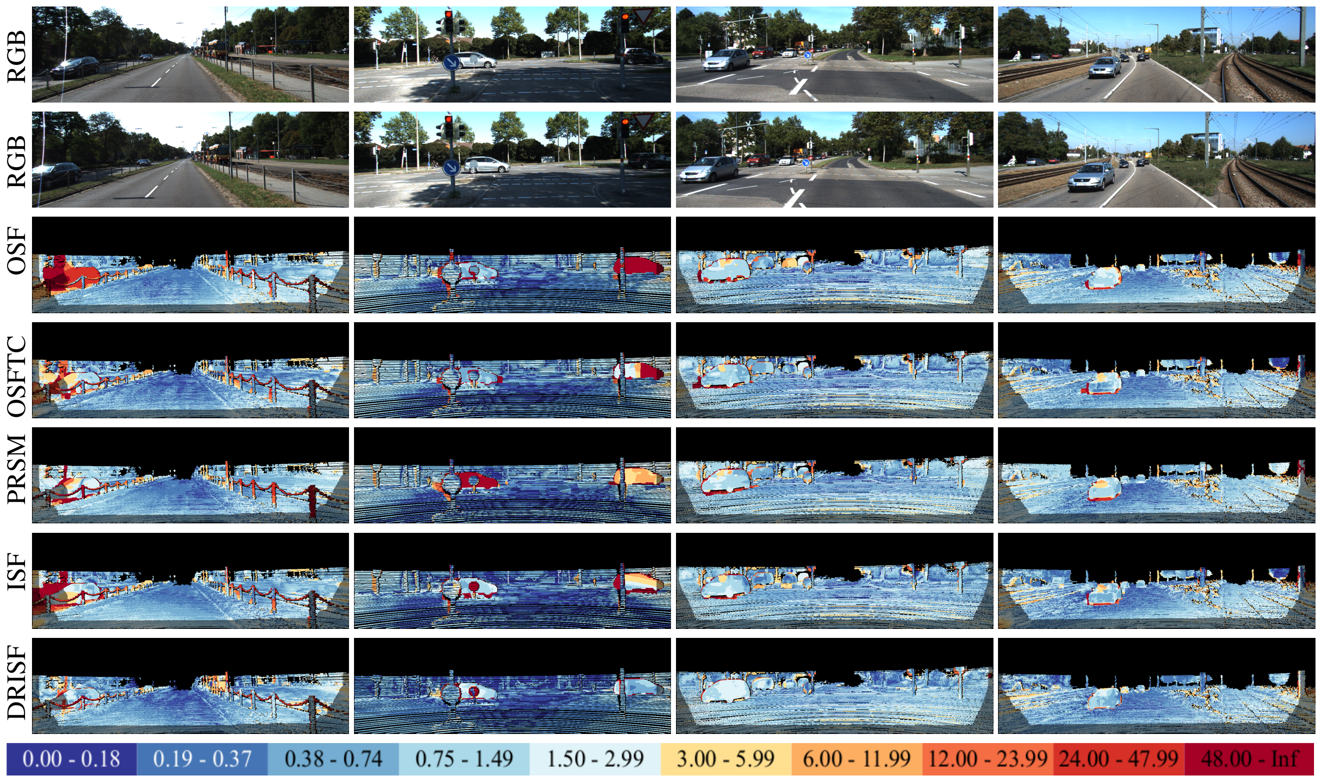

Figure 4: **Qualitative comparison on test sest:** Our method can effecitvely handle occlusion and texture-less regions. It is more robust to the illumination change as well as large displacement.

followed by a rigid transform $\boldsymbol{\xi}$. Specifically,

$$\boldsymbol{p}' = \pi_{\mathbf{K}}(\boldsymbol{\xi} \circ \pi_{\mathbf{K}}^{-1}(\boldsymbol{p}, \mathcal{D}(\boldsymbol{p}))) \tag{3}$$

where $\pi_{\mathbf{K}}(\cdot) : \mathbb{R}^3 \rightarrow \mathbb{R}^2$ is the perspective projection function given known intrinsic $\mathbf{K}$ and $\pi_{\mathbf{K}}^{-1}(\cdot,\cdot) : \mathbb{R}^2 \times \mathbb{R} \rightarrow \mathbb{R}^3$ is the inverse projection that convert a pixel and its associated disparity into a 3D point; $\boldsymbol{\xi} \circ \mathbf{x}$ transforms a 3D point $\mathbf{x}$rigidly with transformation $\exp(\boldsymbol{\xi})\mathbf{x}$. ρ is a robust error function that improves the overall robustness by reducing the influence of outliers on the non-linear least squares problems. Following Sun *et al.* [36], we adopt the generalized Charbonnier function $\rho(x) = (x^2 + \epsilon^2)^\alpha$ as our robust function and set $\alpha = 0.45$ and $\epsilon = 10^{-5}$. Similar to [36], we observe the slightly non-convex penalty improves the performance in practice.

Rigid Fitting: This term encourages the estimated 3D rigid motion to be similar to the point-wise 3D motion obtained from the stereo and flow networks. Formally, given correspondences $\{(\boldsymbol{p}, \boldsymbol{q} = \boldsymbol{p} + F_{\mathcal{L}}(\boldsymbol{p})) | \boldsymbol{p} \in P_i\}$ defined by the output of optical flow network and the disparity maps $\mathcal{D}^0, \mathcal{D}^1$, the energy measures rigid fitting error of $\boldsymbol{\xi}$:

$$E_{\text{rigid},i}(\boldsymbol{\xi}; \mathcal{I}) = \sum_{(\boldsymbol{p},\boldsymbol{q})} \alpha_{\boldsymbol{p}} \rho(\boldsymbol{\xi} \circ \pi_{\mathbf{K}}^{-1}(\boldsymbol{p}, \mathcal{D}^0(\boldsymbol{p})) - \pi_{\mathbf{K}}^{-1}(\boldsymbol{q}, \mathcal{D}^1(\boldsymbol{q}))),$$

where $\boldsymbol{q} = \boldsymbol{p} + \mathcal{F}_{\mathcal{L}}(\boldsymbol{p})$ and $\pi_{\mathbf{K}}^{-1}$ denotes the inverse projection function, and ρ is the same robust error function.

Flow Consistency: This term encourages the projection of the 3D rigid motion to be close to the original flow estimation. This is achieved by measuring the difference between our optical flow net, and the structured rigid flow, which is computed by warping each pixel using $\mathcal{D}^0$ and the rigid motion $\boldsymbol{\xi}$.

$$E_{\text{flow},i}(\boldsymbol{\xi}; \mathcal{I}) = \sum_{\boldsymbol{p} \in P_i} \rho(\underbrace{(\boldsymbol{p}' - \boldsymbol{p})}_{\text{2D Rigid flow}} - \underbrace{\mathcal{F}_{\mathcal{L}}(\boldsymbol{p})}_{\text{optical flow}}) \tag{4}$$

where $\boldsymbol{p}'$ is the rigid warping function defined in Eq. (3), and ρ is the same robust error function.

3.3. Inference

Uncertain Pixel Removal: Due to viewpoint change, flow/stereo prediction errors, etc, the visual cues of some pixels are not reliable. For instance, pixels in one image may be occluded in another image due to viewpoint change. This motivates us to assign $\alpha_{\boldsymbol{p}}$ to each pixel $\boldsymbol{p}$ as an indication of outlier or not. Towards this goal, we first exclude pixels which are likely to be occluded in the next frame.

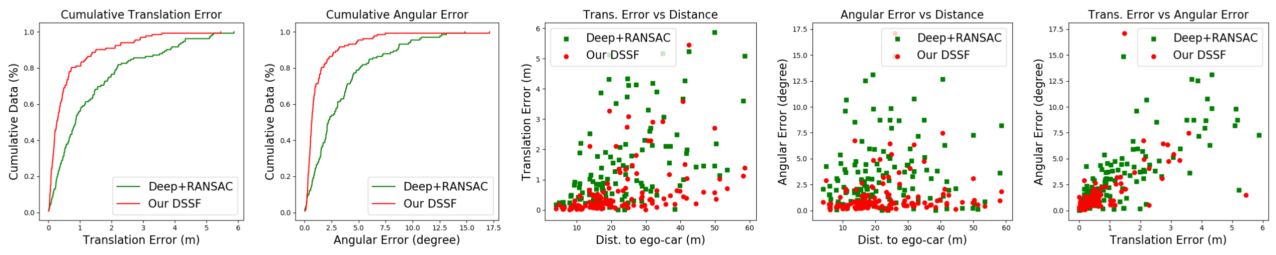

Figure 5: **3D rigid motion analysis:** Over 80% of the estimated 3D rigid motion has an error less than $1m$ and $1.3°$. Large errors often happen at farther distances where the vehicles are small and less points are observable.

Specifically, pixels are labeled as occluded if the warped 3D disparity of the second frame significantly differs from the disparity of the first frame. The intuition is that the disparity of a pixel cannot change drastically in real world due to the speed limit. We empirically set threshold to 30. Next, we employ the RANSAC scheme to fit a rigid motion for each instance. We only keep the inlier points and prune out the rest. Despite simple, we found this strategy very effective.

Initialization: Due to the highly non-convex structure of the energy model, a good initialization is critical to achieve good performance. As previous step already prune out most unreliable points, we directly exploit the rigid motion obtained by RANSAC as our robust initial guess.

Gaussian Newton Solver: The energy function is non-convex but differentiable w.r.t. $\boldsymbol{\xi}$ defined over continuous space. In order to handle the robust function, we adopt an iterative reweighted least square algorithm [8]. For each iteration, we can rewrite the original energy minimization problem of each instance i as a weighted sum of squares:

$$\boldsymbol{\xi}^{(n+1)} = \arg\min_{\boldsymbol{\xi}} E_{\text{total},i}(\boldsymbol{\xi}) = \arg\min_{\boldsymbol{\xi}} \sum_{\text{Eng}} w_i(\boldsymbol{\xi}^{(n)}) r_i^2(\boldsymbol{\xi}^{(n)}),$$

where r denotes the residual function, w reweights each sample based on the robust function ρ, and Eng refers to summing over the energy terms. We employ Gaussian-Newton algorithm to minimize the function. Thus we have

$$\boldsymbol{\xi}^{(n+1)} = \boldsymbol{\xi}^{(n)} \circ (\mathbf{J}^T\mathbf{W}\mathbf{J})^{(-1)}\mathbf{J}^T\mathbf{W}r(\boldsymbol{\xi}^{(n)}) \qquad (5)$$

where $\circ$ is a pose composition operator and $\mathbf{J} = \frac{\delta r(\boldsymbol{\epsilon}\circ\boldsymbol{\xi}^{(n)})}{\delta\boldsymbol{\epsilon}}|_{\boldsymbol{\epsilon}=0}$. In practice, we unroll the inference steps as a recurrent neural network and define its computation graph as in Eq. (5). The full pipeline including the matrix inverse is differentiable. Please refer to the supp. material for the derivation of the Jacobian matrix of each term and more details on the Gaussian-Newton solver.

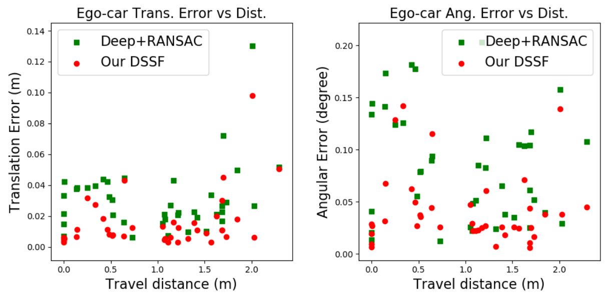

Figure 6: **Odometry from background motion:** On average, our ego-car drifts $1.3cm$ and $0.04°$ every $1m$ of drive.

Final Scene Flow Prediction: Given the final rigid motion estimation for each instance $\boldsymbol{\xi}_i^*$, we are able to compute the dense instance-wise rigid scene flow. Our scene flow consists of three component, namely the first frame's stereo $\mathcal{D}^0$, warped stereo to second frame $\mathcal{D}^{\text{warp}}$ as well as the instance-wise rigid flow estimation $\mathcal{F}^{\text{rigid}}$. Specifically, for each point $\boldsymbol{p}$ we have:

$$\begin{aligned}\mathcal{D}^0(\boldsymbol{p}) &= \mathcal{D}^0(\boldsymbol{p}) \qquad (6)\\ \mathcal{D}^{\text{warp}}(\boldsymbol{p}) &= z_{\mathbf{K}}(\boldsymbol{\xi}^*_{\mathcal{S}^0_{\mathcal{L}}(\boldsymbol{p})} \circ \pi_{\mathbf{K}}^{-1}(\boldsymbol{p}, \mathcal{D}^0(\boldsymbol{p})))\\ \mathcal{F}^{\text{rigid}}(\boldsymbol{p}) &= \boldsymbol{p}' - \boldsymbol{p} = \pi_{\mathbf{K}}(\boldsymbol{\xi} \circ \pi_{\mathbf{K}}^{-1}(\boldsymbol{p}, \mathcal{D}^0(\boldsymbol{p}))) - \boldsymbol{p}\end{aligned}$$

where $z_{\mathbf{K}}(\cdot)$ computes the disparity of the 3D point; $\pi_{\mathbf{K}}^{-1}$ is the inverse projection function; and $\boldsymbol{\xi} \circ \mathbf{x}$ transforms a 3D point $\mathbf{x}$ using the rigid motion $\boldsymbol{\xi}$.

3.4. Learning

The whole deep structured network can be trained end-to-end. In practice, we train our instance segmentation, flow estimation, and stereo estimation module respectively through back-propagation. To be more specific, Mask R-CNN model is pre-trained on Cityscapes and fine-tuned on KITTI. The loss function includes ROI classification loss, box regression loss as well as the mask segmentation loss. PSM-Net is pre-trained on Scene Flow [27] and fine-tuned on KITTI with L1 regression loss. PWC-Net is pre-trained

Employed energy			Background outliers (%)				Employed energy			Foreground outliers (%)			
E_{pho}	E_{flow}	E_{rigid}	D1	D2	Fl	SF	E_{pho}	E_{flow}	E_{rigid}	D1	D2	Fl	SF
✓			1.92	2.69	**3.71**	**4.30**	✓			1.70	**4.25**	7.57	9.00
	✓	✓	1.92	**2.56**	4.72	5.28		✓	✓	1.70	4.58	6.98	8.67
✓	✓	✓	1.92	**2.56**	4.63	5.21	✓	✓	✓	1.70	4.56	**6.73**	**8.39**

Table 2: **Contributions of each energy:** As foreground objects sometimes are texture-less and have large displacement, simple photometric term is not enough. In contrast, background is full of disriminative cues. Simple photometric error would suffice. Adding extra terms will introduce noises and hurt the performance. Please refer to the supp. material for full table.

Methods	D1-all	D2-all	Fl-all	SF-all
PSM + PWC	1.89	(47.0)	11.0	(50.8)
Deep+RANSAC	1.89	**2.75**	7.65	8.26
Our Full DRISF	1.89	2.89	**4.10**	**4.84**

Table 3: **Improvement over original flow/stereo estimation on validation set:** The numbers in parenthis are obtained by simply warping the disparity output with optical flow, without interpolation, occlusion handling, etc.

on FlyingChairs [12] and FlyingThings [27] then fine-tuned over KITTI, with weighted L1 regression loss.

4. Experiments

In this section we first describe the experimental setup. Next we evaluate our model based on pixel-level scene flow metric and instance-level rigid motion metric. Finally we comprehensively study the characteristic of our model.

4.1. Dataset and Implementation Details

Data: We validate our approach on the KITTI scene flow dataset [28]. The dataset consists of 200 sets of training images and 200 sets of test images, captured on real world driving scenarios. Following [9], we divide the training data into *train*, *val* splits based on the 4:1 ratio.

Implementation details: For foreground objects, we use all energy terms. The weights are set to 1. For background, we only use photometric term (see ablation study). We run RANSAC 5 times and use the one with lowest mean energy as initialization. We unroll the GN solver for 50 steps. The solver terminates early if the energy reaches plateau. In practice, best energy are often reached within 10 iterations.

4.2. Scene Flow Estimation

Comparison to the state-of-the-art: We compare our approach against the leading methods on the benchmark[2]:

[2]As the validation performance of our PWC-Net (fine-tuned on 160 images) performs slightly worse than the official one (fine-tuned on all 200 images), we use their weights instead when submitting to the benchmark. All other settings remain intact. We thank Deqing Sun for his help.

Module	Stereo	Optical Flow	Segmentation
Inference time	409 ms / pair	30 ms / pair	251 ms / pair
Module	RANSAC	GN Solver	Total
Inference time	93 ms / instance	244 ms / instance	746 ms / pair

Table 4: **Runtime analysis.** Modules within each building block can be executed in parallel (see text for more details).

ISF [4], PRSM [42], OSF+TC [1], SSF [34], OSF [28], and CSF [26]. Note that in addition to the standard two adjacent frames, PRSM and OSF+TC rely on extra temporal frames. As shown in Tab. 1, our approach (DRISF) outperforms all previous methods by a significant margin in both runtime and outliers ratio. It achieves state-of-the-art performance on almost every entry. DRISF reduces the D1 outliers ratio by **43%**, the D2 outliers ratio by **32%**, and the flow outliers ratio by **24%**. Comparing to ISF model [4], our scene flow error is **22%** lower and our runtime is **800** times faster. Fig. 1 compares the performance and runtime of all methods.

Qualitative results: To better understand the pros and cons of our approach, we visualize a few scene flow results on test set in Fig. 4. Scene flow estimation is challenging in these scenarios due to large vehicle motions, texture-less regions, occlusion, and illumination variation. For the leftmost image, prior methods fail to estimate the vehicle's motion and adjacent area due to the sun reflection and occlusion. The saturated, high intensity pixels hinder photometric based approaches [28] from matching accurately. With the help of detection and segmentation, ISF [4] is able to improve the foreground estimation. Yet it still fails at the occluded background. In comparison, our approach is robust to illumination changes and is able to handle the occlusion by effectively separating the vehicle from the background. It can also accurately estimate the motion of the small car far away, as well as those of the traffic sticks aside. As we only train our Mask R-CNN on vehicles, it fails to segment the train and hence the failure of our model. For the middle image, the texture-less car has a large displacement and is occluded in the second frame. While previous approaches failed substantially, our method is able to produce accurate motion estimation through the inferred flow and disparity of

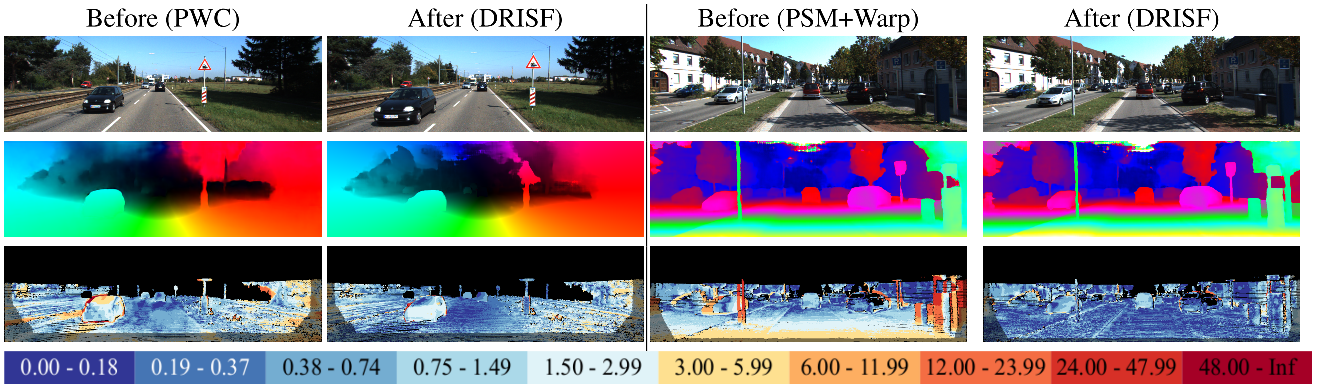

Figure 7: **Improvement over original flow/stereo:** DRISF improves the overall performance. It is especially effective on texture-less regions (*e.g.* window of the black car on the left) and occluded areas (right).

the remaining non-occluded part. The middle failure mode is again due to the inaccurate segmentation.

4.3. 3D Rigid Motion Estimation

We now evaluate how good our DRISF model is at estimating the 3D rigid motion. Towards this goal, we exploit the ground truth optical flow, disparity, and instance segmentation provided in the KITTI scene flow dataset to fit a least square rigid motion for each object instance in order to create the ground truth rigid motion.

Curating KITTI scene flow: During fitting, we discover two critical issues with KITTI: first, there are misalignments between GT flow/disparity and GT segmentation. Second, the scale fitting of the same 3D CAD model employed to compute ground truth changes sometimes across frames. The first issue is due to the fact that the GT are collected via different means and thus not consistent. While the GT flow and GT disparity are obtained from the fitted 3D CAD models, the GT segmentation are based on human annotation. To address this, we first use the GT segmentation mask to define each object instance. We then fit a rigid motion using the GT flow and GT disparity of each instance via least squares. Since some boundary pixels may be mis-labeled by the annotators, for each pixel around the boundary we search if there are other instances in the surrounding area, and if there are, we transform the pixel with their rigid motion. If their rigid motion better explains the pixel's 3D movement, *i.e.* the 3D distance is closer, then we assign the pixel to that instance. At the end, we perform the least square fitting again with the new pixel assignment. Unfortunately, even after re-labeling, there are still a few vehicle instances where the rigid motion cannot be explained. After careful diagnose, we notice that this is because the scale of the CAD model changes across frames. To verify our hypothesis, we compute the eigen decomposition for the same instance across frames. Ideally if the scale of the instance does not change much, the eigen value should be roughly the same. Yet we discover a few examples where the largest eigen value changes by 7%. We simply prune those instances as the GT is not accurate.

3D Motion evaluation: Most scene flow methods are pixel-based or adopted a piece-wise rigid setting. It is unclear how to aggregate their estimation into instance-based motion model without affecting their performance. In light of this, we exploit the motion initialization of our GN Solver as baseline. We take the output of the deep nets and apply RANSAC to find the best rigid motion. We denote it as Deep+RANSAC. As shown in Tab. 3, this baseline is very competitive. Its performance is comparable to, or even better than prior state-of-the-art. We evaluate our motion model based on translation error and angular error. As shown in Fig. 5, over 80% of the vehicles have translation error less than $1m$ and angular error less than $1.3°$. Furthermore, most vehicles with translation error larger than $1m$ is at least $20m$ away. In general, both error slightly increase with distance. This is expected as the farther the vehicle is, the less observations we have. The translation error and angular error are also strongly correlated.

Visual odometry: The odometry of the 'ego-car' can be computed by estimating the background movement. As a proof-of-concept, we compute the per frame odometry error on the validation images. On average our motion model drifts $0.13m$ and $0.4°$ every $10m$. Fig. 6 shows the detailed odometry error w.r.t. the travel distance. We note that the current result is without any pose filter, loop closure, etc. We plan to exploit this direction further in the future.

4.4. Analysis

Ablation study: To understand the effectiveness of each energy term on background and foreground objects, we evaluate our model with different energy combinations. As shown in Tab. 2, best performance is achieved for foreground objects when using all energy terms, while for background the error is lowest when employing only photometric term. This can be explained by the fact that vehicles are often texture-less, and sometimes have large displacements. If we only employ photometric term, it will be very difficult to establish correspondences and handle drastic appearances changes. With the help of flow and rigid term, we can guide the motion and reduce such effect, and deal with occlusions. In contrast, background is full of discriminative textures and has relatively small motion, which is ideal for photometric term. Adding other terms may introduce extra noise and degrade the performance.

Comparison against original flow/disparity: Through exploiting the structure between visual cues and occlusion handling, our model is able to improve the performance both quantitatively (Tab. 3) and qualitatively (Fig. 7). The object motion estimation is better, the boundaries are sharper, and the occlusion error is greatly reduced, suggesting that incorporating prior knowledge, such as pixels of same instance should have same rigid motion, into the model is crucial for the task.

Potential improvement To understand the potential gain we may enjoy when improving each module, we sequentially replace the input to our solver with ground truth, one by one, and evaluate our model. Replacing D1 and flow with GT reduce the scene flow error rate by 8% and 21% respectively, while substituting GT for segmentation does not improve the results. This suggests that there are still space for flow and stereo modules to improve.

Runtime analysis We benchmark the runtime of each component in the model during inference in Tab. 4. The whole inference pipeline can be decomposed into three sequential stages: visual cues extraction, occlusion reasoning, and optimization. As modules within the same stage are independent, they can be executed in parallel. Furthermore, modern self-driving vehicles are equipped with multiple GPUs. The runtime for each stage is thus the max over all parallel modules. In practice, we exploit two Nvidia 1080Ti GPUs to extract the visual cues: one for PSM-Net, and the other for Mask R-CNN and PWC-Net. Currently, the stereo module takes more than 50% of the overall time. This is largely due to the 3D CNN cost aggregation and the stacked hourglass refinement. In the future, we plan to investigate other faster yet reliable stereo networks. The runtime of the GN solver depends highly on the number of steps we unroll and the number of points we consider. Please refer to the supp. material for detailed analysis.

Limitations: DRISF has two main limitations: first, it heavily depends on the performance of the segmentation network. If the segmentation module fails to detect a vehicle, the vehicle will be treated as background and assigned an inverse ego-car motion. In this case, the 3D motion might be completely wrong, even if the optical flow network accurately predicts its flow. In the future we plan to address this by jointly reasoning about instance segmentation and scene flow. Second, the current energy functions are highly flow centric. Only the photometric term is independent of flow. If the optical flow network completely failed, it would be difficult for the solver to recover the correct motion. One possible solution is thus adding more flow-invariant energy terms, such as instance association between adjacent frames.

5. Conclusion

In this paper we develop a novel deep structured model for 3D scene flow estimation. We focus on the self-driving scenario where the motion of the scene can be composed by estimating the 3D rigid motion of each actor. We first exploit deep learning to extract visual cues for each instance. Then we employ multiple geometry based energy functions to encode the structural geometric relationship between them. Through optimizing the energy function, we can reason the 3D motion of each traffic participant, and thus scene flow. All operations, including the Gassian-Newton solver, are done in GPU. Our method acheives state-of-the-art performance on the KITTI scene flow dataset. It outperforms all previous methods by a huge margin in both runtime and accuracy. Comparing to prior art, DRISF is 22% better while being two to three orders of magnitude faster.

References

[1] N. M. Artner, I. Janusch, and W. G. Kropatsch. Object scene flow with temporal consistency. 4, 7

[2] M. Bai, W. Luo, K. Kundu, and R. Urtasun. Exploiting semantic information and deep matching for optical flow. In *ECCV*, 2016. 2

[3] T. Basha, Y. Moses, and N. Kiryati. Multi-view scene flow estimation: A view centered variational approach. *IJCV*, 2013. 3

[4] A. Behl, O. H. Jafari, S. K. Mustikovela, H. A. Alhaija, C. Rother, and A. Geiger. Bounding boxes, segmentations and object coordinates: How important is recognition for 3d scene flow estimation in autonomous driving scenarios? In *ICCV*, 2017. 1, 2, 3, 4, 7

[5] M. Black and T. Anandan. The robust estimation of multiple motions: Parametric and piecewise-smooth flow fields. *CVIU*, 1996. 2

[6] S. Boyd and L. Vandenberghe. *Convex optimization*. Cambridge university press, 2004. 2

[7] T. Brox, A. Bruhn, N. Papenberg, and J. Weickert. High accuracy optical flow estimation based on a theory for warping. In *ECCV*, 2004. 2

[8] E. J. Candes, M. B. Wakin, and S. P. Boyd. Enhancing sparsity by reweighted l1 minimization. *Journal of Fourier analysis and applications*, 2008. 6

[9] J.-R. Chang and Y.-S. Chen. Pyramid stereo matching network. In *CVPR*, 2018. 3, 4, 7

[10] Z. Chen, X. Sun, L. Wang, Y. Yu, and C. Huang. A deep visual correspondence embedding model for stereo matching costs. In *ICCV*, 2015. 2

[11] M. Cordts, M. Omran, S. Ramos, T. Rehfeld, M. Enzweiler, R. Benenson, U. Franke, S. Roth, and B. Schiele. The cityscapes dataset for semantic urban scene understanding. In *CVPR*, 2016. 4

[12] P. Fischer, A. Dosovitskiy, E. Ilg, P. Häusser, C. Hazırbaş, V. Golkov, P. Van der Smagt, D. Cremers, and T. Brox. Flownet: Learning optical flow with convolutional networks. *arXiv*, 2015. 1, 2, 7

[13] A. Geiger, P. Lenz, and R. Urtasun. Are we ready for autonomous driving? the kitti vision benchmark suite. In *Conference on Computer Vision and Pattern Recognition (CVPR)*, 2012. 4

[14] K. He, G. Gkioxari, P. Dollár, and R. Girshick. Mask r-cnn. In *ICCV*, 2017. 3

[15] K. He, X. Zhang, S. Ren, and J. Sun. Spatial pyramid pooling in deep convolutional networks for visual recognition. In *ECCV*, 2014. 3, 4

[16] H. Hirschmuller. Stereo processing by semiglobal matching and mutual information. *TPAMI*, 2008. 2

[17] W. Hoff and N. Ahuja. Surfaces from stereo: Integrating feature matching, disparity estimation, and contour detection. *TPAMI*, 1989. 2

[18] B. K. Horn and B. G. Schunck. Determining optical flow. *Artificial intelligence*, 1981. 2

[19] F. Huguet and F. Devernay. A variational method for scene flow estimation from stereo sequences. In *ICCV*, 2007. 3

[20] T.-W. Hui, X. Tang, and C. C. Loy. Liteflownet: A lightweight convolutional neural network for optical flow estimation. In *CVPR*, 2018. 2

[21] E. Ilg, N. Mayer, T. Saikia, M. Keuper, A. Dosovitskiy, and T. Brox. Flownet 2.0: Evolution of optical flow estimation with deep networks. In *CVPR*, 2017. 2

[22] E. Ilg, T. Saikia, M. Keuper, and T. Brox. Occlusions, motion and depth boundaries with a generic network for disparity, optical flow or scene flow estimation. 2018. 2

[23] T. Kanade and M. Okutomi. A stereo matching algorithm with an adaptive window: Theory and experiment. In *ICRA*, 1991. 2

[24] A. Kendall, H. Martirosyan, S. Dasgupta, P. Henry, R. Kennedy, A. Bachrach, and A. Bry. End-to-end learning of geometry and context for deep stereo regression. 2017. 3

[25] W. Luo, A. G. Schwing, and R. Urtasun. Efficient deep learning for stereo matching. In *CVPR*, 2016. 1, 2

[26] Z. Lv, C. Beall, P. F. Alcantarilla, F. Li, Z. Kira, and F. Dellaert. A continuous optimization approach for efficient and accurate scene flow. In *ECCV*, 2016. 3, 4, 7

[27] N. Mayer, E. Ilg, P. Hausser, P. Fischer, D. Cremers, A. Dosovitskiy, and T. Brox. A large dataset to train convolutional networks for disparity, optical flow, and scene flow estimation. In *CVPR*, 2016. 1, 2, 6, 7

[28] M. Menze and A. Geiger. Object scene flow for autonomous vehicles. In *CVPR*, 2015. 1, 2, 3, 4, 7

[29] A. Newell, K. Yang, and J. Deng. Stacked hourglass networks for human pose estimation. In *ECCV*, 2016. 3

[30] N. Papenberg, A. Bruhn, T. Brox, S. Didas, and J. Weickert. Highly accurate optic flow computation with theoretically justified warping. *IJCV*, 2006. 2

[31] J.-P. Pons, R. Keriven, and O. Faugeras. Multi-view stereo reconstruction and scene flow estimation with a global image-based matching score. *IJCV*, 2007. 3

[32] A. Ranjan and M. J. Black. Optical flow estimation using a spatial pyramid network. In *CVPR*, 2017. 1, 2

[33] S. Ren, K. He, R. Girshick, and J. Sun. Faster r-cnn: Towards real-time object detection with region proposal networks. In *NIPS*, 2015. 4

[34] Z. Ren, D. Sun, J. Kautz, and E. Sudderth. Cascaded scene flow prediction using semantic segmentation. In *3DV*, 2017. 3, 4, 7

[35] J. Revaud, P. Weinzaepfel, Z. Harchaoui, and C. Schmid. Epicflow: Edge-preserving interpolation of correspondences for optical flow. In *CVPR*, 2015. 2

[36] D. Sun, S. Roth, and M. J. Black. Secrets of optical flow estimation and their principles. In *CVPR*, 2010. 5

[37] D. Sun, X. Yang, M.-Y. Liu, and J. Kautz. Models matter, so does training: An empirical study of cnns for optical flow estimation. *arXiv*, 2018. 2

[38] D. Sun, X. Yang, M.-Y. Liu, and J. Kautz. Pwc-net: Cnns for optical flow using pyramid, warping, and cost volume. In *CVPR*, 2018. 1, 2, 4

[39] L. Valgaerts, A. Bruhn, H. Zimmer, J. Weickert, C. Stoll, and C. Theobalt. Joint estimation of motion, structure and geometry from stereo sequences. In *ECCV*, 2010. 3

[40] S. Vedula, S. Baker, P. Rander, R. Collins, and T. Kanade. Three-dimensional scene flow. In *ICCV*, 1999. 1, 3

[41] C. Vogel, K. Schindler, and S. Roth. Piecewise rigid scene flow. In *ICCV*, 2013. 1, 3

[42] C. Vogel, K. Schindler, and S. Roth. 3d scene flow estimation with a piecewise rigid scene model. *IJCV*, 2015. 4, 7

[43] S. Wang, L. Luo, N. Zhang, and J. Li. Autoscaler: Scale-attention networks for visual correspondence. *arXiv*, 2016. 2

[44] K. Yamaguchi, D. McAllester, and R. Urtasun. Efficient joint segmentation, occlusion labeling, stereo and flow estimation. In *ECCV*, 2014. 1, 3

[45] S. Zagoruyko and N. Komodakis. Learning to compare image patches via convolutional neural networks. In *CVPR*, 2015. 2

[46] J. Zbontar and Y. LeCun. Computing the stereo matching cost with a convolutional neural network. In *CVPR*, 2015. 1, 2

[47] J. Zbontar and Y. LeCun. Stereo matching by training a convolutional neural network to compare image patches. *JMLR*, 2016. 2

[48] H. Zhao, J. Shi, X. Qi, X. Wang, and J. Jia. Pyramid scene parsing network. In *CVPR*, 2017. 3, 4

Supplementary Material: Deep Rigid Instance Scene Flow

Abstract

This material provides more details and thorough analysis of our deep rigid instance scene flow (DRISF) model. We hope the readers can gain more insights into our approach. We first provide the derivations of the Jacobians employed in our Gaussian-Newton (GN) solver in Sec. 1. Next, we discuss how the performance and runtime vary with the maximum number of optimization steps in Sec 2. Sec. 4 demonstrates the mis-alignment issue we encounter in the KITTI dataset. Sec 5 showcases more qualitative results as well as a few failure cases. Finally, we provide the screenshot of the leaderboard in Sec. 6.

1. Derivation of the Solver

In this section, we first derive the Jacobian of the energy function in a general form. Then we describe the specific formulation for each term.

1.1. Gauss-Newton Solver

The proposed energy terms can all be expressed in the following form:

$$E(\boldsymbol{\xi};\mathcal{I}) = \sum_{\boldsymbol{p}} \rho(r(\boldsymbol{p},\boldsymbol{\xi};\mathcal{I})),$$

where $\boldsymbol{p}$ refers to the pixels belonging to an instance, ρ is a robust penalty function, and r is a residual function. The goal is to find a transformation $\boldsymbol{\xi}$ that minimizes the energy, or equivalently the sum of square residuals:

$$\boldsymbol{\xi} = \arg\min_{\boldsymbol{\xi}} E(\boldsymbol{\xi};\mathcal{I}) = \arg\min_{\boldsymbol{\xi}} \sum_{\boldsymbol{p}} \rho(r(\boldsymbol{p},\boldsymbol{\xi};\mathcal{I})).$$

As mentioned in the paper, we use the same ρ for all energy terms where $\rho(x) = \tau(x^2) = (x^2+\epsilon^2)^\alpha$.

As the residual function is non-linear and cannot be solved exactly, we iteratively approximate it with a first order Taylor series expansion and search for the local minimum. More formally, the residual function can be approximated as

$$r'(\boldsymbol{p},\Delta\boldsymbol{\xi}) = r(\boldsymbol{p},\boldsymbol{\xi}+\Delta\boldsymbol{\xi};\mathcal{I}) \approx r(\boldsymbol{p},\boldsymbol{\xi};\mathcal{I}) + \frac{\partial r(\boldsymbol{p},\boldsymbol{\xi};\mathcal{I})}{\partial \boldsymbol{\xi}}\Delta\boldsymbol{\xi}.$$

For convenience, we define the Jacobian $\frac{\partial r(\boldsymbol{p},\boldsymbol{\xi};\mathcal{I})}{\partial \boldsymbol{\xi}}$ as $\mathbf{J}_{\boldsymbol{p}}$. Thus we can solve the following surrogate optimization problem instead:

$$\begin{aligned}
\Delta\boldsymbol{\xi}^* &= \arg\min_{\Delta\boldsymbol{\xi}} \sum_{\boldsymbol{p}} \rho(r'(\boldsymbol{p},\Delta\boldsymbol{\xi})) \\
&= \arg\min_{\Delta\boldsymbol{\xi}} \sum_{\boldsymbol{p}} \tau(r'(\boldsymbol{p},\Delta\boldsymbol{\xi})^T r'(\boldsymbol{p},\Delta\boldsymbol{\xi})) \\
&= \arg\min_{\Delta\boldsymbol{\xi}} \sum_{\boldsymbol{p}} \tau((r(\boldsymbol{p},\boldsymbol{\xi}) + \mathbf{J}_{\boldsymbol{p}}\Delta\boldsymbol{\xi})^T (r(\boldsymbol{p},\boldsymbol{\xi}) + \mathbf{J}_{\boldsymbol{p}}\Delta\boldsymbol{\xi}))
\end{aligned}$$

where we simply denote $\rho(x) = \tau(x^2)$. The minimum happens at the point where the gradient is equal to zero. Let us denote $L_{\boldsymbol{p}} = r'(\boldsymbol{p},\Delta\boldsymbol{\xi})^T r'(\boldsymbol{p},\Delta\boldsymbol{\xi})$ and $r'_{\boldsymbol{p}} = r'(\boldsymbol{p},\Delta\boldsymbol{\xi})$. Thus we have:

$$\begin{aligned}
0 &= \frac{\delta E}{\delta \Delta\boldsymbol{\xi}} \\
0 &= \sum_{\boldsymbol{p}} \frac{\delta\tau(L_{\boldsymbol{p}})}{\delta L_{\boldsymbol{p}}} \frac{\delta L_{\boldsymbol{p}}}{\delta r'_{\boldsymbol{p}}} \frac{\delta r'_{\boldsymbol{p}}}{\delta \Delta\boldsymbol{\xi}} \\
0 &= \sum_{\boldsymbol{p}} \frac{\delta\tau(L_{\boldsymbol{p}})}{\delta L_{\boldsymbol{p}}} \cdot 2(r'_{\boldsymbol{p}})^T \cdot \mathbf{J}_{\boldsymbol{p}} \\
0 &= \sum_{\boldsymbol{p}} \frac{\delta\tau(L_{\boldsymbol{p}})}{\delta L_{\boldsymbol{p}}} \cdot 2(r(\boldsymbol{p},\boldsymbol{\xi}) + \mathbf{J}_{\boldsymbol{p}}\Delta\boldsymbol{\xi})^T \cdot \mathbf{J}_{\boldsymbol{p}}
\end{aligned}$$

Since the equation now takes a linear form w.r.t. $\Delta\boldsymbol{\xi}$, we can solve exactly in close form. In particular, the minimum occurs when

$$\sum_{\boldsymbol{p}} \frac{\delta\tau(L_{\boldsymbol{p}})}{\delta L_{\boldsymbol{p}}} \mathbf{J}_{\boldsymbol{p}}^T \mathbf{J}_{\boldsymbol{p}} \Delta\boldsymbol{\xi} = -\sum_{\boldsymbol{p}} \frac{\delta\tau(L_{\boldsymbol{p}})}{\delta L_{\boldsymbol{p}}} \mathbf{J}_{\boldsymbol{p}}^T r(\boldsymbol{p},\boldsymbol{\xi};\mathcal{I}),$$

$$\Delta\boldsymbol{\xi} = -(\sum_{\boldsymbol{p}} \mathbf{J}_{\boldsymbol{p}}^T \mathbf{W}_{\boldsymbol{p}} \mathbf{J}_{\boldsymbol{p}})^{(-1)} \sum_{\boldsymbol{p}} \mathbf{J}_{\boldsymbol{p}}^T \mathbf{W}_{\boldsymbol{p}} r(\boldsymbol{p},\boldsymbol{\xi};\mathcal{I}),$$

where $\mathbf{W}$ is a diagonal matrix with diagonal entries equal to $\frac{\delta\tau(L_{\boldsymbol{p}})}{\delta L_{\boldsymbol{p}}}$. We hence take a step and update the transformation $\boldsymbol{\xi} \leftarrow \boldsymbol{\xi} \circ \Delta\boldsymbol{\xi}$.

We next describe the residual function and the Jacobian for each term. We use the same notations as in the paper. We further define $\mathbf{x} = \begin{bmatrix} x & y & z \end{bmatrix}^T = \boldsymbol{\xi} \circ \pi_{\mathbf{K}}^{-1}(\boldsymbol{p}, \mathcal{D}(\boldsymbol{p}))$ as the 3D coordinate of the pixel $\boldsymbol{p}$ after inverse depth warping and applying rigid transform $\boldsymbol{\xi}$.

1.2. Jacobian of Each Energy Term

Photometric error: The residual function of the photometric error is simply the RGB pixel value difference. Formally, it is defined as:

$$r(\boldsymbol{p}, \boldsymbol{\xi}; \mathcal{I}) = \mathcal{L}^1(\boldsymbol{p}') - \mathcal{L}^0(\boldsymbol{p}).$$

The Jacobian is defined as:

$$\begin{aligned}\mathbf{J} = \frac{\partial r(\boldsymbol{p}, \boldsymbol{\xi}; \mathcal{I})}{\partial \boldsymbol{\xi}} &= \frac{\partial \mathcal{L}^1(\boldsymbol{p}') - \mathcal{L}^0(\boldsymbol{p})}{\partial \boldsymbol{\xi}} \\ &= \frac{\partial \mathcal{L}^1(\boldsymbol{p}')}{\partial \boldsymbol{p}'} \frac{\partial \pi_{\mathbf{K}}(\mathbf{x})}{\partial \mathbf{x}} \frac{\partial \mathbf{x}}{\partial \boldsymbol{\xi}} \\ &= \begin{bmatrix} \nabla_x \mathcal{L}^1 \\ \nabla_y \mathcal{L}^1 \end{bmatrix} \begin{bmatrix} \frac{f_x}{z} & 0 & -\frac{x f_x}{z^2} \\ 0 & \frac{f_y}{z} & -\frac{y f_y}{z^2} \end{bmatrix} \begin{bmatrix} 1 & 0 & 0 & 0 & z & -y \\ 0 & 1 & 0 & -z & 0 & x \\ 0 & 0 & 1 & y & -x & 0 \end{bmatrix}\end{aligned}$$

Rigid fitting: The residual function of the rigid fitting term is simply the 3D distance between the 3D point and its correspondence. Formally, it is defined as:

$$\begin{aligned}r(\boldsymbol{p}, \boldsymbol{\xi}; \mathcal{I}) &= \boldsymbol{\xi} \circ \pi_{\mathbf{K}}^{-1}\left(\boldsymbol{p}, \mathcal{D}^0(\boldsymbol{p})\right) - \pi_{\mathbf{K}}^{-1}\left(\boldsymbol{q}, \mathcal{D}^1(\boldsymbol{q})\right) \\ &= \mathbf{x} - \pi_{\mathbf{K}}^{-1}\left(\boldsymbol{q}, \mathcal{D}^1(\boldsymbol{q})\right).\end{aligned}$$

The Jacobian is thus:

$$\begin{aligned}\mathbf{J} = \frac{\partial r(\boldsymbol{p}, \boldsymbol{\xi}; \mathcal{I})}{\partial \boldsymbol{\xi}} &= \frac{\partial \mathbf{x} - \pi_{\mathbf{K}}^{-1}\left(\boldsymbol{q}, \mathcal{D}^1(\boldsymbol{q})\right)}{\partial \boldsymbol{\xi}} \\ &= \frac{\partial \mathbf{x}}{\partial \boldsymbol{\xi}} = \begin{bmatrix} 1 & 0 & 0 & 0 & z & -y \\ 0 & 1 & 0 & -z & 0 & x \\ 0 & 0 & 1 & y & -x & 0 \end{bmatrix}\end{aligned}$$

Flow consistency: The residual function of the flow consistency term is simply the difference between the estimated flow and the projection of the estimated 3D motion. Formally, it is defined as:

$$r(\boldsymbol{p}, \boldsymbol{\xi}; \mathcal{I}) = (\boldsymbol{p}' - \boldsymbol{p}) - \mathcal{F}_{\mathcal{L}}(\boldsymbol{p}).$$

The Jacobian is defined as:

$$\begin{aligned}\mathbf{J} &= \frac{\partial (\boldsymbol{p}' - \boldsymbol{p}) - \mathcal{F}_{\mathcal{L}}(\boldsymbol{p})}{\partial \boldsymbol{\xi}} = \frac{\partial \boldsymbol{p}'}{\partial \boldsymbol{\xi}} = \frac{\partial \boldsymbol{p}'}{\partial \mathbf{x}} \frac{\partial \mathbf{x}}{\partial \boldsymbol{\xi}} \\ &= \frac{\partial \pi_{\mathbf{K}}(\mathbf{x})}{\partial \mathbf{x}} \frac{\partial \mathbf{x}}{\partial \boldsymbol{\xi}} \\ &= \begin{bmatrix} \frac{f_x}{z} & 0 & -\frac{x f_x}{z^2} \\ 0 & \frac{f_y}{z} & -\frac{y f_y}{z^2} \end{bmatrix} \begin{bmatrix} 1 & 0 & 0 & 0 & z & -y \\ 0 & 1 & 0 & -z & 0 & x \\ 0 & 0 & 1 & y & -x & 0 \end{bmatrix}\end{aligned}$$

2. Impact of Unrolling Steps in GN Solver

In this section, we study the trade-off between performance and runtime with respect to the maximum number of unrolling steps in the GN solver. As shown in Fig. 1, our model can achieve very good performance within 10 steps. The overall performance still improves a bit as the optimization procedure proceeds, since a few foreground instances require longer time to converge. In practice, many instances converge within 10 steps, which leads to the speed boost in Fig. 2. To gain more intuition, we also visualize the scene flow error map at different iterations in Fig. 3. For more qualitative results, we refer the readers to the attached video.

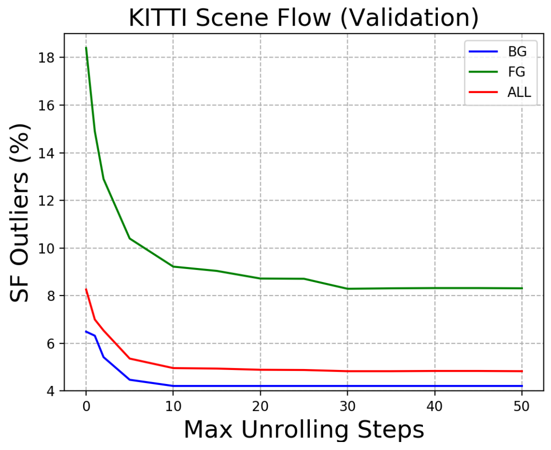

Figure 1: **Performance vs unrolling steps.** While foreground requires 30 steps to converge, background achieves best results within 10 steps. As a consequence, the overall performance reaches plateau after 10 steps, with only minor improvement. We note that despite the foreground outliers reduce quite a bit after 10 steps, it is mainly caused by a few instances. Most instances converges within 10 steps.

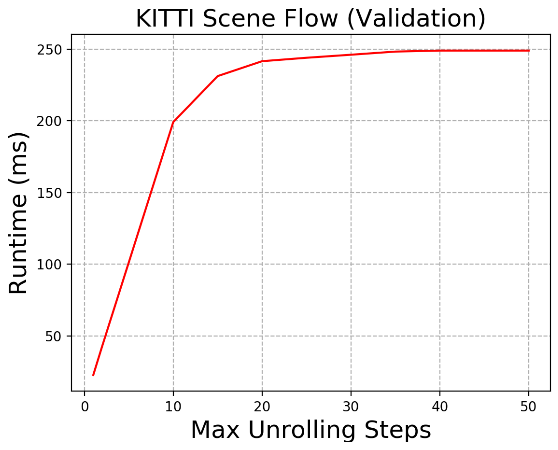

Figure 2: **Runtime vs unrolling steps.** At first the runtime scales linearly with the maximum number of steps. As more instances converge (*i.e.* the energy reaches plateau) and terminate, the runtime becomes faster.

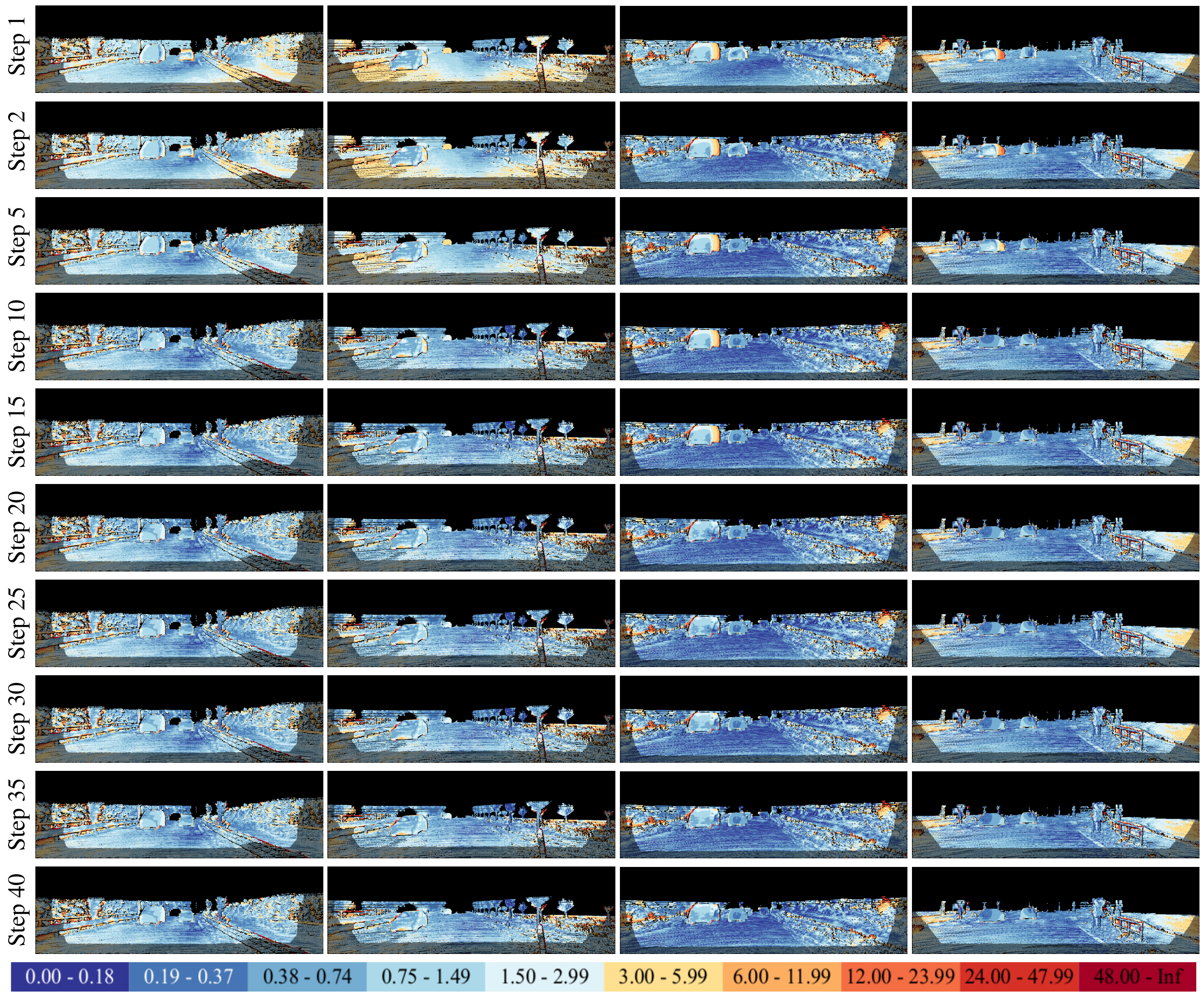

Figure 3: **Scene flow error at different GN iterations.** At first the estimated foreground motion is not accurate (see the orange/red cars in the first row). With our carefully designed energy terms, we are able to handle the outliers in the inferred visual cues and recover the accurate motion (see how the cars gradually turn into blue). *Click the image to see the gif animation.*

3. Impact of energy functions

To understand the effectiveness of each energy term on background and foreground objects, we evaluate our model with different energy combinations. The full ablation table is shown in Tab. 1. While best performance is achieved for foreground objects when using all energy terms, the error is lowest for background when employing only photometric term. This can be explained by the fact that vehicles are often texture-less, and sometimes have large displacements. If we only employ photometric term, it will be very difficult to establish correspondences and handle drastic appearances changes. With the help of flow and rigid term, we can guide the motion and reduce such effect, and deal with occlusions. In contrast, background is full of discriminative textures and has relatively small motion, which is ideal for photometric term. Adding other terms may introduce extra noise and degrade the performance.

4. Curating KITTI Scene Flow

While creating the instance-wise 3D rigid motion ground truth (GT) from KITTI scene flow dataset, we discover two critical issues: firstly, there are mis-alignments over instance boundaries between the GT scene flow and GT instance segmentation; secondly, we find that the scale of the

Employed energy			Background outliers (%)				Employed energy			Foreground outliers (%)			
E_{pho}	E_{flow}	E_{rigid}	D1	D2	Fl	SF	E_{pho}	E_{flow}	E_{rigid}	D1	D2	Fl	SF
✓			1.92	2.69	**3.71**	**4.30**	✓			1.70	4.25	7.57	9.00
	✓		1.92	2.57	4.73	5.31		✓		1.70	5.53	8.39	10.5
		✓	1.92	2.59	5.92	6.45			✓	1.70	3.72	14.9	16.1
✓	✓		1.92	2.57	4.25	4.82	✓	✓		1.70	5.18	7.97	9.85
	✓	✓	1.92	2.56	4.72	5.28		✓	✓	1.70	4.58	6.98	8.67
✓		✓	1.92	**2.55**	4.69	5.25	✓		✓	1.70	**3.70**	7.98	9.24
✓	✓	✓	1.92	2.56	4.63	5.21	✓	✓	✓	1.70	4.56	**6.73**	**8.39**

Table 1: **Contributions of each energy:** As foreground objects sometimes are texture-less and have large displacement, simple photometric term is not enough. In contrast, background is full of discriminative cues. Simple photometric error would suffice. Adding extra terms will introduce noises and hurt the performance.

same 3D instance changes across two frames, which is impossible in practice.

Fig. 4 shows two examples where the GT scene flow and GT segmentation mis-align. For each pixel, we determine its scene flow based instance label by finding if its scene flow better fits the rigid motion of a foreground instance or the background scene. We also get another source of labels from instance segmentation task. If a point is defined as foreground instance by both scene flow and the instance segmentation, it is colored in yellow. It is colored in green/red if only the scene flow/segmentation indicates it belongs to foreground object. If both agree it is background, we colored it in blue. In general, the mis-alignment happens at the boundaries. It is expected as the amount of CAD models (employed to compute GT flow/disparity) and their underlying transformations are limited and it is difficult to cover all types of cars on the road while GT instance are labeled by humans through polygons. The mis-alignment will also result in incorrect rigid motion[1], especially when there are many outliers. We thus *re-label* the points and compute the rigid motion again. This greatly reduces the outliers ratio.

Even after fixing the instance boundary mis-alignment issue, we find it is still difficult to fit a rigid transform for a few instances that makes GT flow and GT disparity agree with each other. We suspect this is due to the fact that some instances do not undergo rigid transform in the data. To solidify our claim, we further compute the 3D distance between the same pair of points from an instance at different time step. To be more specific, we obtain the correspondences at different frames using GT flow and exploit GT disparity to compute their respective 3D coordinates. As shown in Fig. 5, the 3D distance between the points changes quite a bit for the vehicle. It seems like the underlying transformation across the frames is not rigid. We verify with the authors [4] and they confirm that an additional scale parameter is employed to fit the 3D CAD model to each frame independently during the GT creation stage. Several objects thus do not undergo a rigid transform. To address this, we simply treat them as don't care regions, and ignore them when computing our metrics.

[1]As there are no GT for the rigid motion, we evaluate its quality using the scene flow metric. To be more specific, we use the GT D1 and the fitted rigid motion to compute scene flow via Eq. 6 and measure the number of outliers.

5. Qualitative Results

Fig. 6 and Fig. 7 provide more qualitative comparison against the baselines. Fig. 8 and Fig. 9 show a few examples where our model fails.

6. KITTI Scene Flow Benchmark

Fig. 10 shows the screenshot of the KITTI scene flow leaderboard at the time of paper submission. Our method outperforms all previous methods, including anonymous submissions, by a significant margin in both runtime and performance.

References

[1] N. M. Artner, I. Janusch, and W. G. Kropatsch. Object scene flow with temporal consistency. 6

[2] A. Behl, O. H. Jafari, S. K. Mustikovela, H. A. Alhaija, C. Rother, and A. Geiger. Bounding boxes, segmentations and object coordinates: How important is recognition for 3d scene flow estimation in autonomous driving scenarios? In *ICCV*, 2017. 6, 7

[3] Z. Lv, C. Beall, P. F. Alcantarilla, F. Li, Z. Kira, and F. Dellaert. A continuous optimization approach for efficient and accurate scene flow. In *ECCV*, 2016. 6

[4] M. Menze and A. Geiger. Object scene flow for autonomous vehicles. In *CVPR*, 2015. 4, 6, 7

[5] Z. Ren, D. Sun, J. Kautz, and E. Sudderth. Cascaded scene flow prediction using semantic segmentation. In *3DV*, 2017. 6

[6] T. Taniai, S. N. Sinha, and Y. Sato. Fast multi-frame stereo scene flow with motion segmentation. In *CVPR*, 2017. 6

[7] C. Vogel, K. Schindler, and S. Roth. Piecewise rigid scene flow. In *ICCV*, 2013. 6, 7

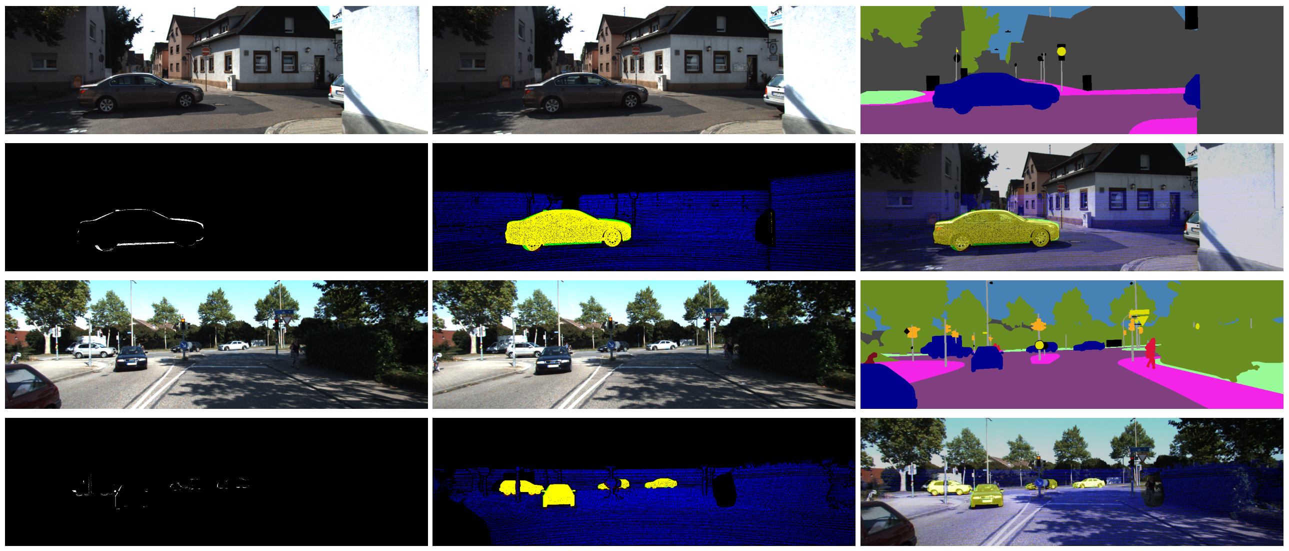

Figure 4: **Mis-alignment between the GT scene flow instance and the GT segmentation.** We show two examples of the mis-alignment. A point is colored in yellow if both scene flow instance and GT segmentation agree it is foreground. Red means only segmentation agrees, and green suggests only scene flow instance agrees. A point is blue is both agree it is background. Points where the two disagree are shown in white in bottom left.

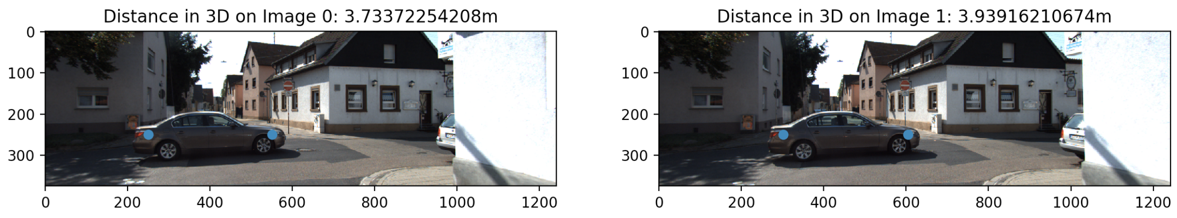

Distance in 3D on Image 0: 3.73372254208m
Distance in 3D on Image 1: 3.93916210674m
0
100
200
300
0
200
400
600
800
1000
1200

Figure 5: **Instances does not follow rigid transform.** The 3D distance between exact same two points changes across frames. The distance increases by 5.4% within 0.1 second which is quite significant. Note that 3D position and correspondence are computed using GT disparity and GT flow.

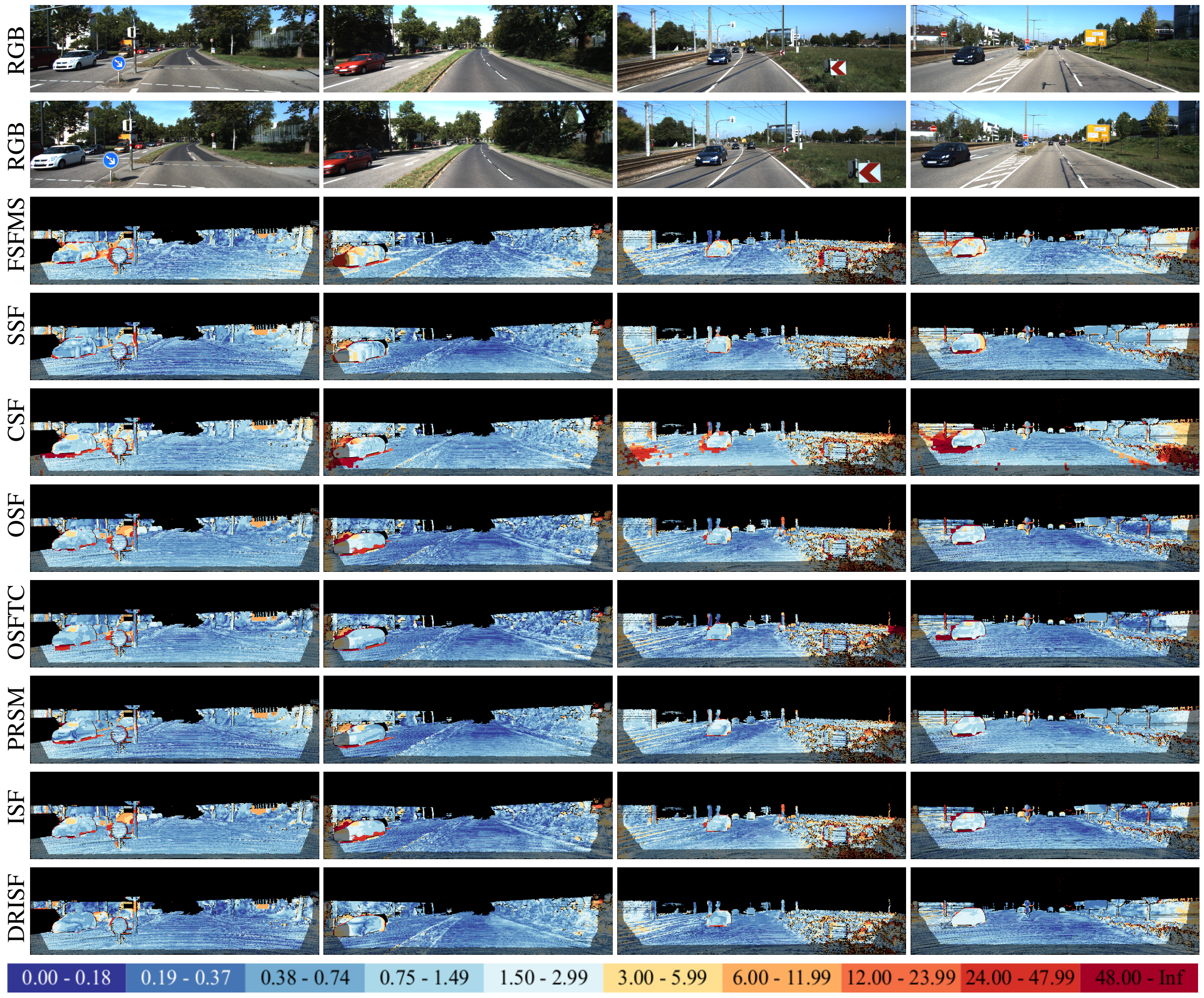

Figure 6: **Qualitative comparison on test set.** We compare with the competitive, top leading methods on KITTI leaderboard: FSFMS [6], SSF [5], CSF [3], OSF [4], OSFTC [1], PRSM [7], ISF [2]. Our method can effectively handle occlusion and texture-less regions. It is more robust to the illumination change as well as large displacement.

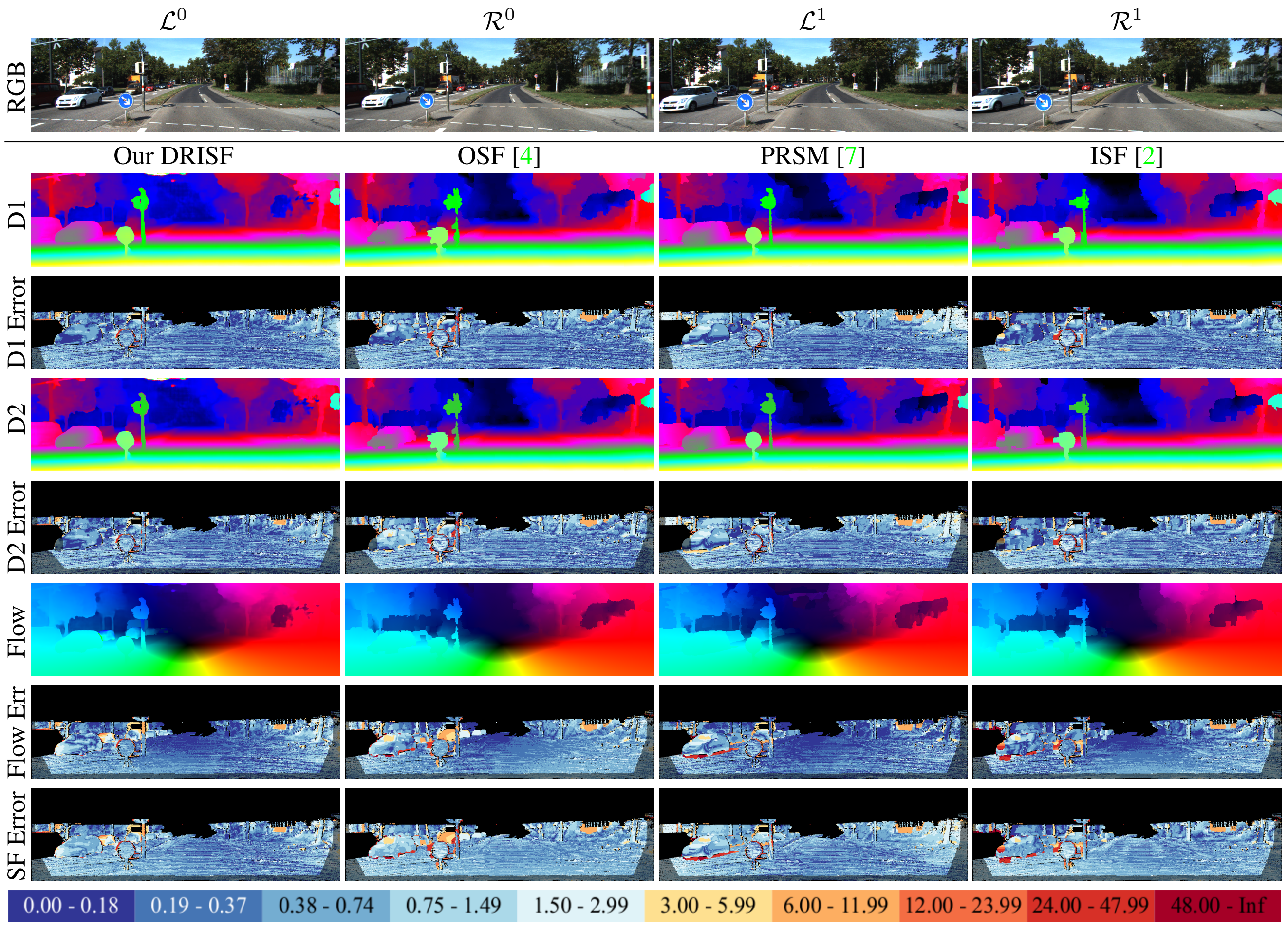

Figure 7: **Qualitative comparison on test set.** We visualize the results and error maps of each component of OSF [4], PRSM [7], and ISF [2]. Our method can effectively handle occlusion and texture-less regions. It is more robust to the illumination change as well as large displacement.

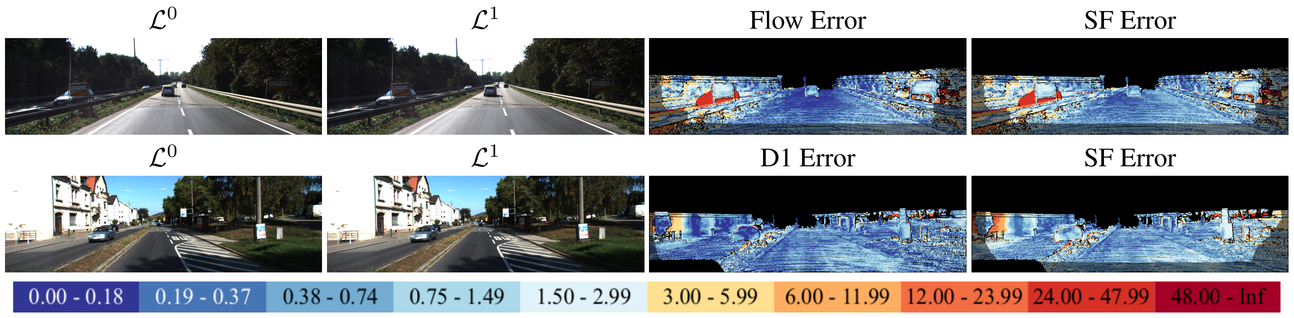

Figure 8: **Failure case of the scene flow model.** Our energy model takes the inferred visual cues (*i.e.* flow, disparity) as input. If the original estimation is completely wrong, our model fails to recover the actual motion. In the first row, the flow estimation of the largely occluded vehicle is completely wrong. For background, the flow error has less impact, as we can recover its motion from other reliable background points. It however still relies heavily on D1 (see Eq. 6 in the paper). If D1 estimation is incorrect, our model can hardly work. To address this issue and avoid being bounded by the visual cues, we plan to optimize both the disparity and flow in the solver. We leave this for future study.

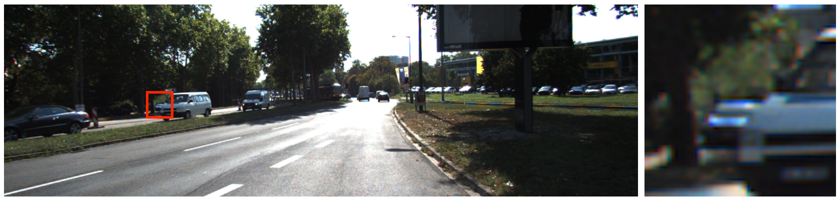

Figure 9: **Failure case of the inferred 3D rigid motion model.** The small blue car is partially occluded by the white van in the first frame, and is completely invisible in the second. The estimated visual cues are thus completely wrong (unlike background it cannot benefit from other observations). It leads to 5 m translation error and 17.5 degree angular error.

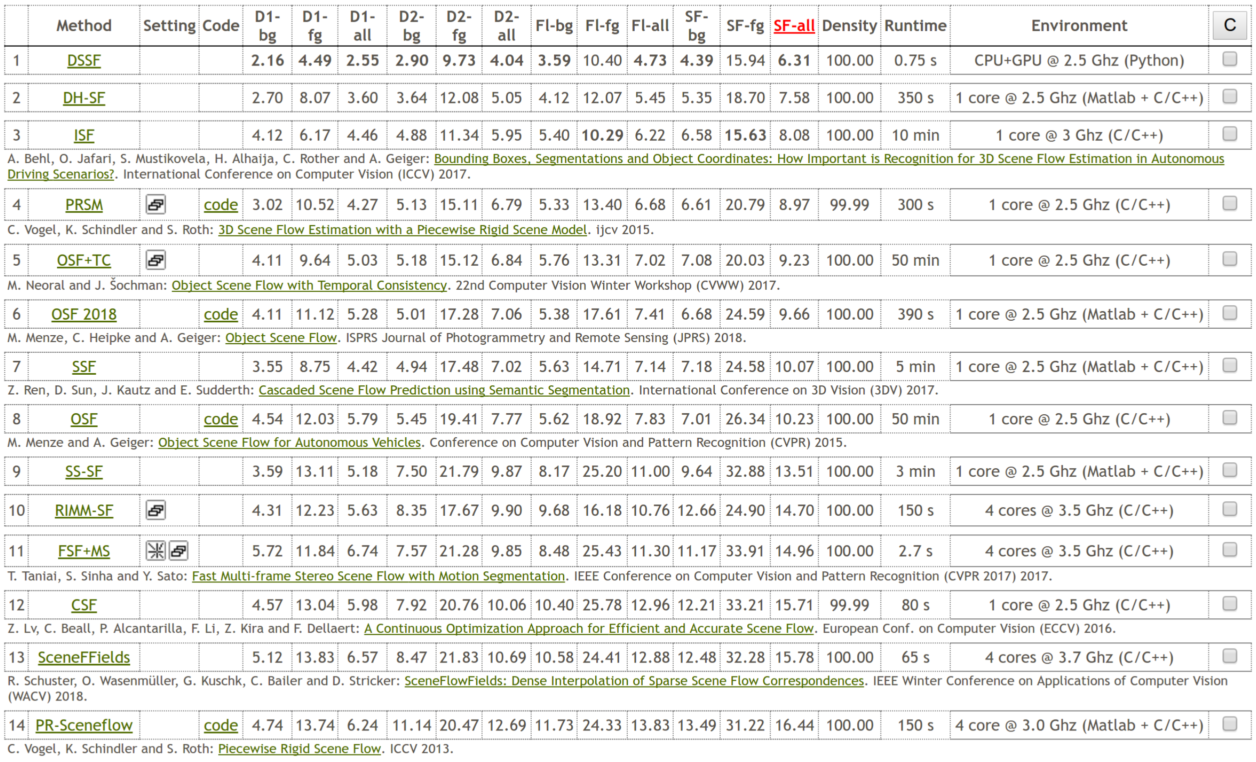

	Method	Setting	Code	D1-bg	D1-fg	D1-all	D2-bg	D2-fg	D2-all	Fl-bg	Fl-fg	Fl-all	SF-bg	SF-fg	SF-all	Density	Runtime	Environment	C
1	DSSF			**2.16**	**4.49**	**2.55**	**2.90**	**9.73**	**4.04**	**3.59**	10.40	**4.73**	**4.39**	15.94	**6.31**	100.00	0.75 s	CPU+GPU @ 2.5 Ghz (Python)	☐
2	DH-SF			2.70	8.07	3.60	3.64	12.08	5.05	4.12	12.07	5.45	5.35	18.70	7.58	100.00	350 s	1 core @ 2.5 Ghz (Matlab + C/C++)	☐
3	ISF			4.12	6.17	4.46	4.88	11.34	5.95	5.40	**10.29**	6.22	6.58	**15.63**	8.08	100.00	10 min	1 core @ 3 Ghz (C/C++)	☐
	A. Behl, O. Jafari, S. Mustikovela, H. Alhaija, C. Rother and A. Geiger: Bounding Boxes, Segmentations and Object Coordinates: How Important is Recognition for 3D Scene Flow Estimation in Autonomous Driving Scenarios?. International Conference on Computer Vision (ICCV) 2017.																		
4	PRSM	⧉	code	3.02	10.52	4.27	5.13	15.11	6.79	5.33	13.40	6.68	6.61	20.79	8.97	99.99	300 s	1 core @ 2.5 Ghz (C/C++)	☐
	C. Vogel, K. Schindler and S. Roth: 3D Scene Flow Estimation with a Piecewise Rigid Scene Model. ijcv 2015.																		
5	OSF+TC	⧉		4.11	9.64	5.03	5.18	15.12	6.84	5.76	13.31	7.02	7.08	20.03	9.23	100.00	50 min	1 core @ 2.5 Ghz (C/C++)	☐
	M. Neoral and J. Šochman: Object Scene Flow with Temporal Consistency. 22nd Computer Vision Winter Workshop (CVWW) 2017.																		
6	OSF 2018		code	4.11	11.12	5.28	5.01	17.28	7.06	5.38	17.61	7.41	6.68	24.59	9.66	100.00	390 s	1 core @ 2.5 Ghz (Matlab + C/C++)	☐
	M. Menze, C. Heipke and A. Geiger: Object Scene Flow. ISPRS Journal of Photogrammetry and Remote Sensing (JPRS) 2018.																		
7	SSF			3.55	8.75	4.42	4.94	17.48	7.02	5.63	14.71	7.14	7.18	24.58	10.07	100.00	5 min	1 core @ 2.5 Ghz (Matlab + C/C++)	☐
	Z. Ren, D. Sun, J. Kautz and E. Sudderth: Cascaded Scene Flow Prediction using Semantic Segmentation. International Conference on 3D Vision (3DV) 2017.																		
8	OSF		code	4.54	12.03	5.79	5.45	19.41	7.77	5.62	18.92	7.83	7.01	26.34	10.23	100.00	50 min	1 core @ 2.5 Ghz (C/C++)	☐
	M. Menze and A. Geiger: Object Scene Flow for Autonomous Vehicles. Conference on Computer Vision and Pattern Recognition (CVPR) 2015.																		
9	SS-SF			3.59	13.11	5.18	7.50	21.79	9.87	8.17	25.20	11.00	9.64	32.88	13.51	100.00	3 min	1 core @ 2.5 Ghz (Matlab + C/C++)	☐
10	RIMM-SF	⧉		4.31	12.23	5.63	8.35	17.67	9.90	9.68	16.18	10.76	12.66	24.90	14.70	100.00	150 s	4 cores @ 3.5 Ghz (C/C++)	☐
11	FSF+MS	✳ ⧉		5.72	11.84	6.74	7.57	21.28	9.85	8.48	25.43	11.30	11.17	33.91	14.96	100.00	2.7 s	4 cores @ 3.5 Ghz (C/C++)	☐
	T. Taniai, S. Sinha and Y. Sato: Fast Multi-frame Stereo Scene Flow with Motion Segmentation. IEEE Conference on Computer Vision and Pattern Recognition (CVPR 2017) 2017.																		
12	CSF			4.57	13.04	5.98	7.92	20.76	10.06	10.40	25.78	12.96	12.21	33.21	15.71	99.99	80 s	1 core @ 2.5 Ghz (C/C++)	☐
	Z. Lv, C. Beall, P. Alcantarilla, F. Li, Z. Kira and F. Dellaert: A Continuous Optimization Approach for Efficient and Accurate Scene Flow. European Conf. on Computer Vision (ECCV) 2016.																		
13	SceneFFields			5.12	13.83	6.57	8.47	21.83	10.69	10.58	24.41	12.88	12.48	32.28	15.78	100.00	65 s	4 cores @ 3.7 Ghz (C/C++)	☐
	R. Schuster, O. Wasenmüller, G. Kuschk, C. Bailer and D. Stricker: SceneFlowFields: Dense Interpolation of Sparse Scene Flow Correspondences. IEEE Winter Conference on Applications of Computer Vision (WACV) 2018.																		
14	PR-Sceneflow		code	4.74	13.74	6.24	11.14	20.47	12.69	11.73	24.33	13.83	13.49	31.22	16.44	100.00	150 s	4 core @ 3.0 Ghz (Matlab + C/C++)	☐
	C. Vogel, K. Schindler and S. Roth: Piecewise Rigid Scene Flow. ICCV 2013.																		

Figure 10: **Screenshot of the KITTI scene flow leaderboard at the time of paper submission.** Our model (named DSSF previously) achieves state-of-the-art performance on almost every entry (**bold**) while being significantly faster.